J. Fluid Mech. (1983), *vol.* 132, *pp.* 231–245
Printed in Great Britain

Temperature-gradient-driven electrohydrodynamic instability with unipolar injection in air

By JAMES F. HOBURG

Department of Electrical Engineering, Carnegie-Mellon University, Pittsburgh, Pennsylvania 15213

(Received 19 July 1982)

Electrohydrodynamic instability is described in a planar region of gas, with unipolar injection through a linear temperature gradient, with corresponding mobility, viscosity, and density gradients. The role of charge-relaxation instability, which is incipient at a critical value of electric Rayleigh number in a uniform mobility layer, is distinguished from the mobility-gradient-driven mechanism, which can produce instability at much smaller voltage thresholds. Relative values of electroviscous time, viscous diffusion time and ion transit time determine the nature of the instability process. The instability is stationary or dynamic for wavenumbers respectively below or above a critical value. The fastest-growing wavenumber and corresponding growth rate are determined as functions of time constants and temperature gradient.

1. Introduction

The ability of an ion flux from a high-voltage electrical discharge to augment heat transfer from a heated object in a gas has been recognized at least as far back as a 1933 U.S. patent for cooling of the exterior casing of stepdown transformers (Palueff 1933). Since then, a variety of applications have involved the same fundamental mechanism – augmentation of heat transfer in a gas, usually air, by means of an ion flux, typically from a corona-discharge electrode (Sadek 1969; McDermott 1971; Lindsley 1973; Kibler 1974; Kibler & Carter 1974; Kulacki & Daumenmier 1978).

Understanding of the nature of the interactions involved in such processes is somewhat clouded by the simultaneous involvement of more than one physical mechanism. The most obvious and often cited effect is that associated with the so-called 'corona wind', wherein collisions between field-driven ions and neutral air molecules result in a net drift of the medium within which the current flux is imposed (Chattock 1899; Robinson 1961). Thus, the electrical discharge has an effect somewhat similar to that of a conventional fan in driving air motion in regions adjacent to the heated surface. (The large difference between ion and ambient gas speeds points to the relative inefficiency of this process – a fan is a much more effective means of causing bulk gas motions.)

A less obvious mechanism, which motivates the model described here, derives from the dependence of electrical mobility on temperature. Adjacent to a heated surface, a gradient in temperature implicitly involves a gradient in electrical mobility. The resultant electric field variation and its associated space-charge accumulation drive a bulk-coupled electrohydrodynamic instability, with attendant mixing processes similar to those driven by conductivity gradients in ohmic liquids (Hoburg & Melcher 1976, 1977; Hoburg 1978). The efficiency of the mobility-gradient-driven mechanism

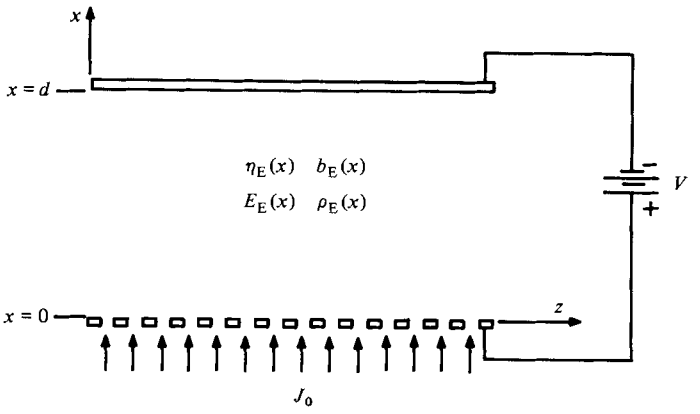

FIGURE 1. One-dimensional model. A unipolar ion flux is injected into a planar layer with vertically varying equilibrium mobility, viscosity and mass density.

in producing fine-scale mixing at the scale of mobility variations motivates the analysis described in this paper.

Considerable attention has been given to an instability process which can result from injection of a unipolar ion flux into an insulating region with imposed potential difference between electrodes (Schneider & Watson 1970; Watson, Schneider & Till 1970; Atten & Moreau 1970; Hopfinger & Grosse 1971; Atten & Lacroix 1978). Like the mechanism described above, this process involves the accumulation of space charge in a spatially varying electric field, and consequent instability dynamics. Unlike the mobility-gradient-driven mechanism, this process can occur in a region of uniform mobility, provided the applied potential difference exceeds a threshold value. It is not associated with the scale of a property gradient. This kind of instability will be referred to below as 'classical' space-charge EHD instability. As described explicitly in §5, different dimensionless groups govern instability growth through classical and mobility-gradient-driven mechanisms. A part of the purpose of this paper is an unravelling of these distinct mechanisms as a means of understanding their relative importances and effects.

A relatively recent investigation has produced a description of incipience of a stationary EHD instability driven by a temperature-induced mobility variation with unipolar injection (Worraker & Richardson 1979). Because that analysis refers specifically to a dielectric liquid, mechanical properties, including viscosity, are taken as constant. In this paper, where the interest is in augmentation of heat transfer in a gaseous medium, a temperature-induced mobility gradient involves simultaneous viscosity and density gradients. It is shown here that the instability is stationary or dynamic for wavenumbers respectively below or above a critical value. The nature of instability growth and structure is documented as a function of relevant time-constant parameters and for currents less than the space-charge-limited value.

2. Equilibrium structure

The model shown in figure 1 involves a planar region of gas which is electrically highly insulating. Electrical conduction through the region comes about due to injection of a unipolar charge species at the lower boundary and application of a high

potential difference between upper and lower boundaries. In order to isolate the fundamental physical mechanism of interest, the geometry is purely one-dimensional – equilibrium physical variables are functions only of the vertical (x) dimension.

The layer has uniform permittivity ϵ and vertically varying equilibrium mobility $b_{\mathrm{E}}(x)$. A vertical current density $J_0 \boldsymbol{i}_x$ is injected at the lower boundary ($x = 0$), leading to equilibrium electric field $E_{\mathrm{E}}(x)\boldsymbol{i}_x$ and charge density $\rho_{\mathrm{E}}(x)$. The equilibrium structure is determined by steady-state conservation of charge, which requires $\rho_{\mathrm{E}}(x)\, b_{\mathrm{E}}(x)\, E_{\mathrm{E}}(x) = J_0$, a constant, and by Gauss' Law, which requires $\epsilon\, \mathrm{d}E_{\mathrm{E}}(x)/\mathrm{d}x = \rho_{\mathrm{E}}(x)$.

If the imposed potential difference across the layer of thickness d is V, normalized variables are defined by

$$\bar{b}_{\mathrm{E}}(x) = \frac{b_{\mathrm{E}}(x)}{b_0}, \tag{1}$$

where

$$b_0 \equiv b_{\mathrm{E}}(0),$$

$$\bar{\rho}_{\mathrm{E}}(x) = \frac{\rho_{\mathrm{E}}(x)\, d^2}{\epsilon V}, \tag{2}$$

$$\bar{E}_{\mathrm{E}}(x) = \frac{E_{\mathrm{E}}(x)\, d}{V}, \tag{3}$$

$$\bar{x} = \frac{x}{d}, \tag{4}$$

$$\bar{J}_0 = \frac{J_0 d^3}{\epsilon b_0 V^2}, \tag{5}$$

$$\bar{\Psi}(\bar{x}) = \int_0^{\bar{x}} \frac{\mathrm{d}\xi}{\bar{b}_{\mathrm{E}}(\xi)}. \tag{6}$$

The imposed potential difference determines the electric field at $\bar{x} = 0$, $\bar{E}_0 \equiv \bar{E}_{\mathrm{E}}(0)$, for a specified injected current density and mobility variation

$$1 = \int_0^1 (\bar{E}_0^2 + 2\bar{J}_0\, \bar{\Psi})^{\frac{1}{2}}\, \mathrm{d}\bar{x}, \tag{7}$$

where $\bar{J}_0$ must be less than a space-charge-limited value

$$\bar{J}_{\mathrm{SCL}} = \frac{1}{2}\left[\int_0^1 \bar{\Psi}^{\frac{1}{2}}\, \mathrm{d}\bar{x}\right]^{-2}. \tag{8}$$

The equilibrium electric field and charge distributions, then, are

$$\bar{E}_{\mathrm{E}} = (\bar{E}_0^2 + 2\bar{J}_0\, \bar{\Psi})^{\frac{1}{2}}, \tag{9}$$

$$\bar{\rho}_{\mathrm{E}} = \frac{\bar{J}_0}{\bar{b}_{\mathrm{E}}} (\bar{E}_0^2 + 2\bar{J}_0\, \bar{\Psi})^{-\frac{1}{2}}. \tag{10}$$

If the model shown in figure 1 refers specifically to a static equilibrium where the upper electrode is hot, the temperature increases linearly with x. In terms of a normalized temperature $\bar{T}(\bar{x})$, defined such that $\bar{T}(0) \equiv 1$ and $\bar{T}(1) \equiv \bar{T}_1$, then,

$$\bar{T} = 1 + (\bar{T}_1 - 1)\, \bar{x}. \tag{11}$$

Following Worraker & Richardson (1979) a simple linear dependence of mobility

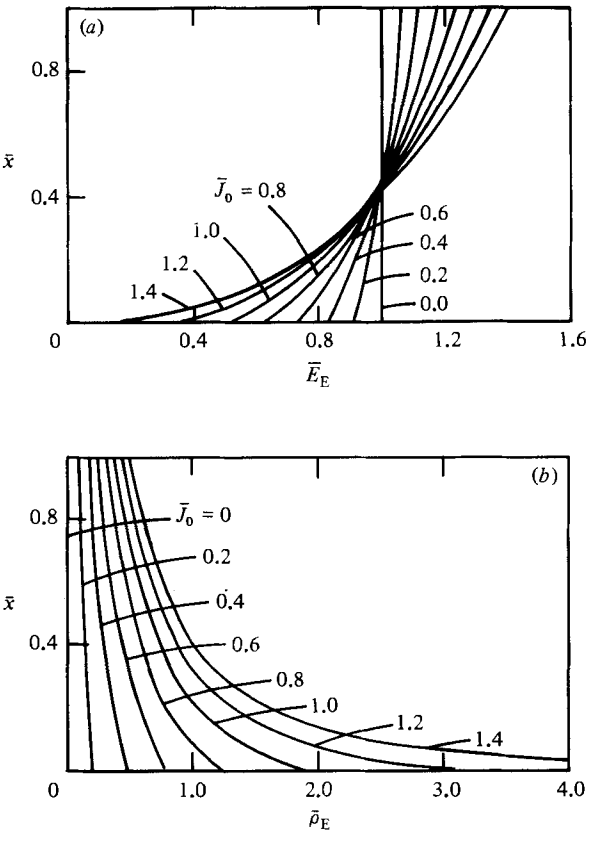

FIGURE 2. Equilibrium electric-field and charge-density structures for injected currents less than the space-charge-limited value in a linearly varying temperature and hence mobility distribution. The upper plate is at normalized temperature $\bar{T}_1 = 1.75$. $\bar{E}_E(\bar{x})$ and $\bar{\rho}_E(\bar{x})$ are reduced from constant-mobility values to an increasing degree as mobility increases. (*a*) Equilibrium electric field $\bar{E}_E(\bar{x})$. (*b*) Equilibrium charge density $\bar{\rho}_E(\bar{x})$.

on temperature is taken to represent the first-order term of a more complex dependence. The dependence of normalized mobility on position, then, is

$$\bar{b}_E(\bar{x}) = 1 + \kappa(\bar{T}_1 - 1)\,\bar{x}, \tag{12}$$

where, for air with the lower electrode at 293 K, $\kappa = 1.36$ (Cobine 1958). The corresponding $\bar{\Psi}(\bar{x})$, from (6), is

$$\bar{\Psi}(\bar{x}) = \frac{1}{\kappa(\bar{T}_1 - 1)} \ln\left(1 + \kappa[\bar{T}_1 - 1]\,\bar{x}\right). \tag{13}$$

Figure 2 shows $\bar{E}_E(\bar{x})$ and $\bar{\rho}_E(\bar{x})$ for the linearly varying mobility distribution with $\bar{T}_1 = 1.75$. For this case, the space-charge-limited current is $\bar{J}_{SCL} = 1.4292$, as compared with a value of $\bar{J}_{SCL} = 1.1250$ in the constant-mobility ($\bar{T}_1 = 1.00$) case. The obvious effect of the mobility gradient is to reduce equilibrium electric field and charge density from their constant mobility distributions to an increasing degree with increasing $\bar{x}$, and to permit higher injected current densities.

The equilibrium mechanical properties of the layer are viscosity $\eta_E(x)$ and density $\rho_R(x)$. Each is normalized to its value at $x = 0$:

$$\bar{\eta}_{\mathrm{E}}(x) = \frac{\eta_{\mathrm{E}}(x)}{\eta_0}, \quad \bar{\rho}_{\mathrm{R}}(x) = \frac{\rho_{\mathrm{R}}(x)}{\rho_0}, \tag{14), (15}$$

where $\eta_0 \equiv \eta_{\mathrm{E}}(0)$ and $\rho_0 \equiv \rho_{\mathrm{R}}(0)$.

The variation of viscosity with temperature is represented, in a manner analogous to that used for mobility, with a simple linear dependence. The dependence of normalized viscosity on position, then, takes the form

$$\bar{\eta}_{\mathrm{E}}(\bar{x}) = 1 + \lambda(\bar{T}_1 - 1)\,\bar{x}, \tag{16}$$

where, for air with the lower electrode at 293 K, $\lambda = 0.60$ (Weast 1970).

Finally, density varies inversely with absolute temperature (Weast 1970), and hence the dependence of normalized density on position is given by

$$\bar{\rho}_{\mathrm{R}}(\bar{x}) = \frac{1}{1 + [\bar{T}_1 - 1]\,\bar{x}}. \tag{17}$$

3. Perturbation dynamics

The following laws govern relationships among the physical variables of concern in the model represented by figure 1. With fluid mass density ρ_{m}, viscosity η, velocity components, v_i, stress-tensor components S_{ij}, electric charge density ρ_{f}, electric field components E_i, and pressure p, taking an acoustic wavelength to be long enough for times of interest to model the fluid as incompressible, the Navier–Stokes equations are

$$\rho_{\mathrm{m}}\left(\frac{\partial v_i}{\partial t} + v_j \frac{\partial v_i}{\partial x_j}\right) = \rho_{\mathrm{f}} E_i + \frac{\partial S_{ij}}{\partial x_j}, \tag{18}$$

$$S_{ij} = -p\delta_{ij} + \eta\left(\frac{\partial v_i}{\partial x_j} + \frac{\partial v_j}{\partial x_i}\right), \tag{19}$$

$$\frac{\partial v_j}{\partial x_j} = 0. \tag{20}$$

Provided that fluid viscosity η, density ρ_{m}, and mobility b diffuse slowly compared with times characterizing instability dynamics, the convective derivative of each quantity vanishes:

$$\frac{\partial \eta}{\partial t} + \boldsymbol{v}\cdot\boldsymbol{\nabla}\eta = 0, \tag{21}$$

$$\frac{\partial \rho_{\mathrm{m}}}{\partial t} + \boldsymbol{v}\cdot\boldsymbol{\nabla}\rho_{\mathrm{m}} = 0, \tag{22}$$

$$\frac{\partial b}{\partial t} + \boldsymbol{v}\cdot\boldsymbol{\nabla}b = 0. \tag{23}$$

The electroquasistatic electric field is curl-free, and has the charge density as a source in Gauss' Law:

$$\boldsymbol{\nabla}\times\boldsymbol{E} = 0, \tag{24}$$

$$\boldsymbol{\nabla}\cdot\epsilon\boldsymbol{E} = \rho_{\mathrm{f}}. \tag{25}$$

Finally, conservation of charge, with current density given by $\rho_{\mathrm{f}}(b\boldsymbol{E} + \boldsymbol{v})$, yields

$$\boldsymbol{\nabla}\cdot(\rho_{\mathrm{f}}[b\boldsymbol{E} + \boldsymbol{v}]) + \frac{\partial \rho_{\mathrm{f}}}{\partial t} = 0. \tag{26}$$

The stability of the electromechanical system is determined mathematically by expressing each physical quantity as the sum of equilibrium and perturbation parts, where perturbation variables are taken to have time and horizontal spatial dependences of the form $\xi^* e^{(st-ikz)}$, where ξ^* is a complex amplitude. The objective of a stability analysis, then, is the determination of the dispersion relation between complex growth rate s and spatial wavenumber k. Substitution of the physical variable forms into (18)–(26) and assumption of perturbation magnitudes small enough to justify linearization yields a system of 12 equations in the 12 unknown perturbation magnitudes. Algebraic elimination of η^*, ρ_m^*, b^*, p^*, and S_{zz}^* then leaves a system of 7 equations in 7 unknowns.

The system may be written in terms of governing time constants and normalized variables defined as follows:

$$\tau_E = \frac{\eta_0 d^2}{\epsilon V^2}, \quad \tau_M = \frac{\rho_0 d^2}{\eta_0}, \quad \tau_I = \frac{d^2}{b_0 V}, \tag{27}$$

$$[\bar{v}_x^*, \bar{v}_z^*] = \frac{\eta_0 d}{\epsilon V^2}[v_x^*, v_z^*], \tag{28}$$

$$[\bar{S}_{xx}^*, \bar{S}_{xz}^*] = \frac{d^2}{\epsilon V^2}[S_{xx}^*, S_{xz}^*], \tag{29}$$

$$[\bar{E}_x^*, \bar{E}_z^*] = \frac{d}{V}[E_x^*, E_z^*], \tag{30}$$

$$\bar{\rho}_f^* = \frac{d^2}{\epsilon V}\rho_f^*, \tag{31}$$

$$\bar{k} = kd, \quad \bar{s} = s\tau_E, \quad \bar{D} = d\frac{d}{dx}. \tag{32}$$

The seven coupled linear, first-order, non-constant-coefficient differential equations relating normalized perturbation amplitudes are then

$$\bar{D}\bar{v}_z^* = \frac{\bar{S}_{xz}^*}{\bar{\eta}_E} + i\bar{k}\bar{v}_x^*, \tag{33}$$

$$\bar{D}\bar{v}_x^* = i\bar{k}\bar{v}_z^*, \tag{34}$$

$$\bar{D}\bar{E}_z^* = -i\bar{k}\bar{E}_x^*, \tag{35}$$

$$\bar{D}\bar{E}_x^* = i\bar{k}\bar{E}_z^* + \bar{\rho}_f^*, \tag{36}$$

$$\bar{D}\bar{S}_{xz}^* = i\bar{k}\bar{S}_{xx}^* + \left[4\bar{\eta}_E\bar{k}^2 + \frac{\bar{s}\tau_M}{\tau_E}\bar{\rho}_R\right]\bar{v}_z^* - \bar{\rho}_E\bar{E}_z^*, \tag{37}$$

$$\bar{D}\bar{S}_{xx}^* = i\bar{k}\bar{S}_{xz}^* + \frac{\bar{s}\tau_M}{\tau_E}\bar{\rho}_R\bar{v}_x^* - \bar{\rho}_E\bar{E}_x^* - \bar{E}_E\bar{\rho}_f^*, \tag{38}$$

$$\bar{D}\bar{\rho}_f^* = \frac{1}{\bar{b}_E\bar{s}}\left(\bar{\rho}_E\bar{D}^2\bar{b}_E + \frac{\bar{D}\{\bar{\rho}_E\bar{E}_E\}\bar{D}\bar{b}_E}{\bar{E}_E} - \frac{\bar{s}\tau_I}{\tau_E}\frac{\bar{D}\bar{\rho}_E}{\bar{E}_E}\right)\bar{v}_x^*$$
$$+\left(\frac{i\bar{k}\bar{\rho}_E\bar{D}\bar{B}_E}{\bar{s}\bar{b}_E}\right)\bar{v}_z^* - \left(\frac{\bar{D}\{\bar{\rho}_E\bar{b}_E\}}{\bar{b}_E\bar{E}_E}\right)\bar{E}_x^* - \frac{1}{\bar{E}_E}\left(\frac{\bar{D}\{\bar{b}_E\bar{E}_E\}}{\bar{b}_E} + \bar{\rho}_E + \frac{\bar{s}\tau_I/\tau_E}{\bar{b}_E}\right)\bar{\rho}_f^*. \tag{39}$$

For the configuration of figure 1, if superscripts α and β are associated with the upper and injection electrodes respectively, then the boundary conditions on

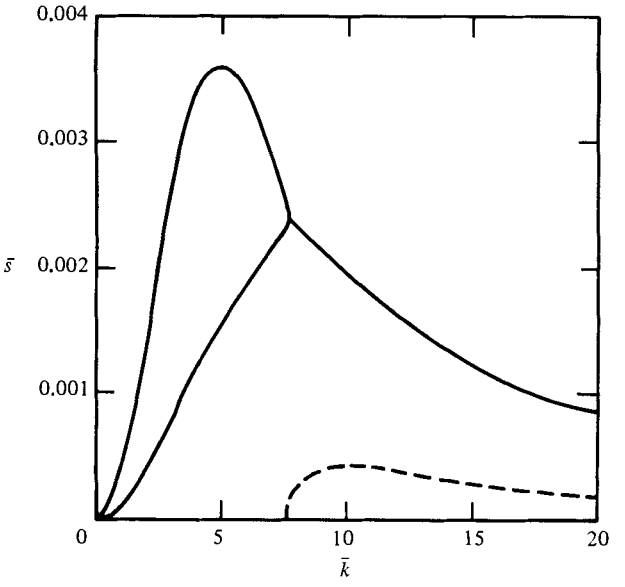

FIGURE 3. Two fastest-growing eigenfrequencies as functions of wavenumber with $\bar{T}_1 = 1.75$, $\bar{J}_0 = 1.0, \tau_M/\tau_E = 1.0$, and $\tau_I/\tau_E = 0$. The fastest-growing eigenfrequency reaches a maximum value $\bar{s}^*$ at wavenumber k^*. The two roots merge at a higher value of k, then become a complex-conjugate pair, corresponding to propagation at short wavelengths. Real and imaginary parts are denoted by solid and dashed lines, respectively.

perturbation velocity and electric field components are:

$$[\bar{v}_x^{*\alpha} = \bar{v}_z^{*\alpha} = \bar{E}_z^{*\alpha} = \bar{v}_x^{*\beta} = \bar{v}_z^{*\beta} = \bar{E}_z^{*\beta} = 0. \tag{40}$$

The seventh boundary condition derives from the nature of current injection at the lower electrode. For an injected current density less than the space-charge-limited value, the injected charge density is taken as independent of perturbation dynamics, and thus

$$\bar{\rho}_f^{*\beta} = 0. \tag{41}$$

(This boundary condition, through $\bar{E}_z^{*\beta} = 0$ and (36), is equivalent to $D\bar{E}_x^{*\beta} = 0$, as used by Atten & Moreau (1976) for 'autonomous injection'.)

Determination of eigenfrequencies $\bar{s}$ for specified wavenumbers $\bar{k}$, time-constant ratios τ_M/τ_E and τ_I/τ_E, and equilibrium variable distributions involves a technique which has been successfully applied in the context of similarly modelled systems (Hoburg & Melcher 1976; Hoburg 1978). A Runga–Kutta integration procedure is used to determine the components of the 7×3 matrix, $\boldsymbol{L}$, defined by:

$$[\bar{v}_z^{*\alpha}, \bar{v}_x^{*\alpha}, \bar{E}_z^{*\alpha}, \bar{E}_x^{*\alpha}, \bar{S}_{xz}^{*\alpha}, \bar{S}_{xx}^{*\alpha}, \bar{\rho}_f^{*\alpha}]^T = \boldsymbol{L}[\bar{E}_x^{*\beta}, \bar{S}_{xz}^{*\beta}, \bar{S}_{xx}^{*\beta}]^T. \tag{42}$$

(The first three boundary conditions in (40) and (41) have been incorporated here.) Among the entries in $\boldsymbol{L}$ are the components of the 3×3 matrix $\boldsymbol{T}$, defined by

$$[\bar{v}_z^{*\alpha}, \bar{v}_x^{*\alpha}, \bar{E}_z^{*\alpha}]^T = \boldsymbol{T}[\bar{E}_x^{*\beta}, \bar{S}_{xz}^{*\beta}, \bar{S}_{xx}^{*\beta}]^T. \tag{43}$$

Thus the dispersion relation necessary to satisfy the last three boundary conditions in (40) is

$$\det \boldsymbol{T} = 0. \tag{44}$$

An iterative search procedure in the complex $\bar{s}$-plane is used to find the eigenfrequency solutions (Hoburg 1978).

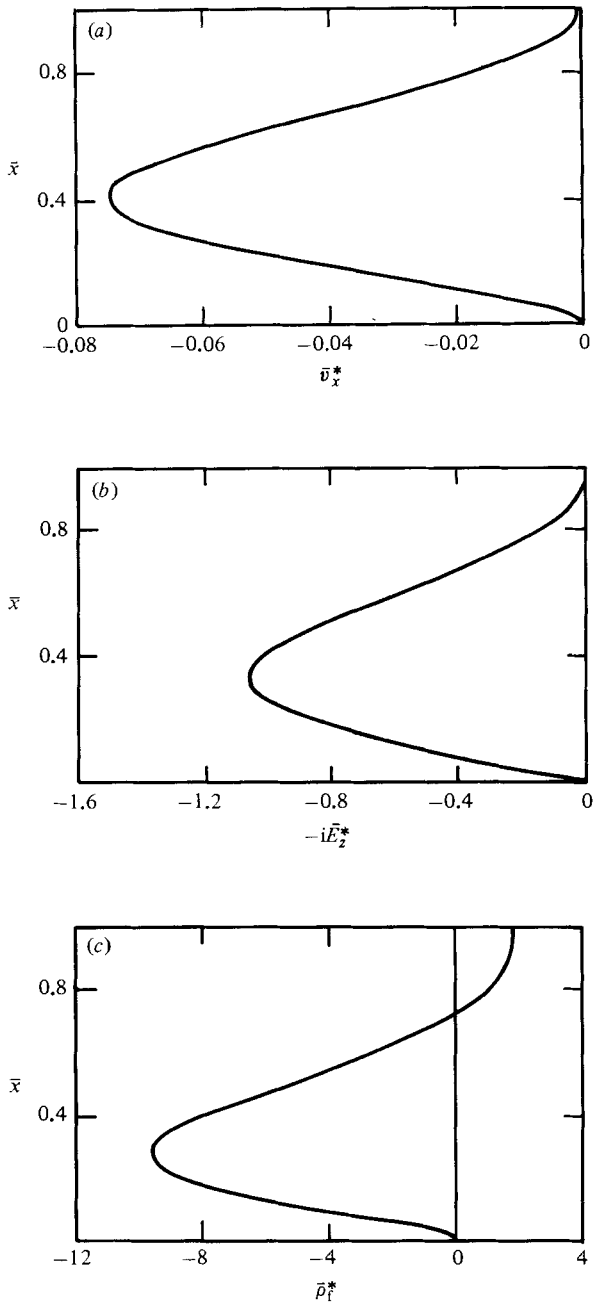

FIGURE 4. Perturbation variables as functions of position at the fastest-growing eigenfrequency of figure 3. (*a*) Perturbation vertical velocity, $\bar{v}_x^*$. (*b*) Perturbation horizontal electric field, $\bar{E}_z^*$. (*c*) Perturbation charge density, $\bar{\rho}_f^*$.

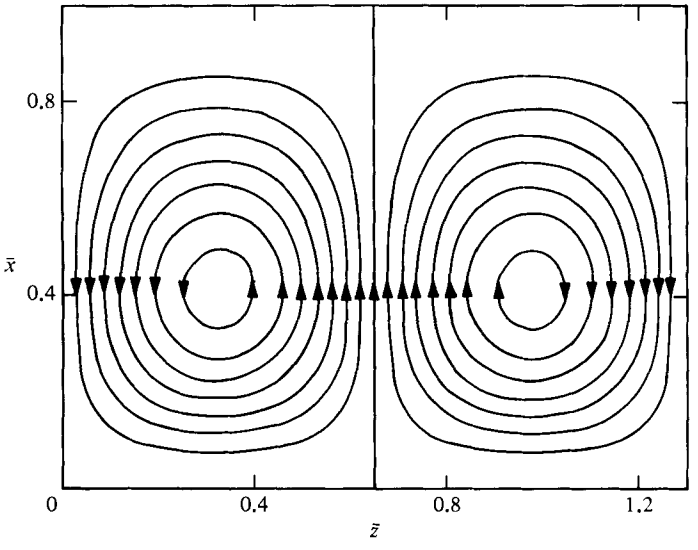

(*a*)

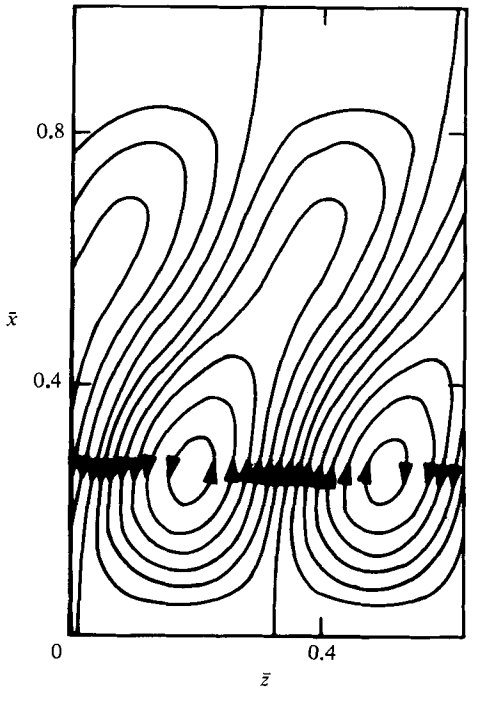

(*b*)

FIGURE 5. Cellular fluid streamlines for stationary and propagating eigenfrequencies. The transition from real to complex roots corresponds to a change from stationary vertical cells to propagating slanted cells. (*a*) Stationary streamlines at the fastest-growing eigenfrequency of figure 3. (*b*) Propagating streamlines at $\bar{k} = 10$ in figure 3.

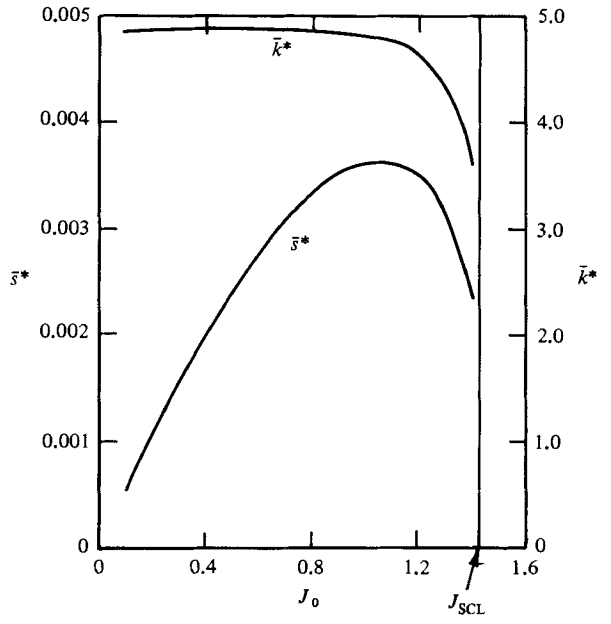

FIGURE 6. Fastest-growing wavenumber k^* and growth rate $\bar{s}^*$ as functions of injected current density $\bar{J}_0$ with $\bar{T}_1 = 1.75$, $\tau_M/\tau_E = 1.0$, and $\tau_1/\tau_E = 0$. $\bar{k}^*$ is nearly constant for $\bar{J}_0$ much less than the space-charge-limited value, then decreases as $\bar{J}_0$ nears $\bar{J}_{SCL}$. $\bar{s}^*$ has a maximum at a value of $\bar{J}_0$ less than $\bar{J}_{SCL}$, indicating most-rapid growth at sub-space-charge-limited conditions.

4. Results

Figure 3 shows the behaviour of the two fastest-growing eigenfrequencies as functions of wavenumber $\bar{k}$. The dependence is similar to that found in a model for EHD instability in a region with a collinear applied field and conductivity gradient (Hoburg 1978). Both eigenfrequencies are positive and pure real, starting at the origin and increasing with increasing $\bar{k}$. The fastest growing eigenfrequency reaches a maximum value, termed $\bar{s}^*$, at $\bar{k} = \bar{k}^*$, then decreases to meet the still-rising second eigenfrequency. Here, the two zeros of det $\boldsymbol{T}$ merge on the real $\bar{s}$-axis, and with further increases in $\bar{k}$ become a conjugate pair in the complex $\bar{s}$-plane. Thus, the instability, which is stationary for long wavelengths, becomes oscillatory for short wavelengths. (Real and imaginary parts of the complex eigenfrequencies are represented by solid and dashed lines respectively in figure 3.)

The nature of the instability described by the eigenfrequency solutions represented in figure 3 is clarified by the corresponding eigenfunction distributions. At a value of $\bar{s}$ where (44) is satisfied, linear combinations of the elements of $\boldsymbol{T}$ yield values of $\bar{S}^{*\beta}_{xz}$ and $\bar{S}^{*\beta}_{zx}$ corresponding to an arbitrarily set $\bar{E}^{*\beta}_x = 1 + \mathrm{i}0$. Numerical integration of the governing equations (33)–(39) across the layer then determines the distributions of the perturbation variables, and vanishing values of $\bar{v}^*_x$, $\bar{v}^*_z$ and $\bar{E}^*_z$ at $\bar{x} = 1$ confirm the eigenfrequency solution. Figure 4 shows the perturbation variables $\bar{v}^*_x$, $\bar{E}^*_z$ and $\bar{\rho}^*_f$ as functions of position across the layer at the fastest-growing eigenfrequency in figure 3. Less rapidly growing eigenfrequencies at the same wavenumber correspond to more variations of the eigenfunctions across the layer.

In figure 5, fluid streamlines are plotted corresponding to the fastest-growing eigenfrequency and corresponding to a complex eigenfrequency at a relatively high

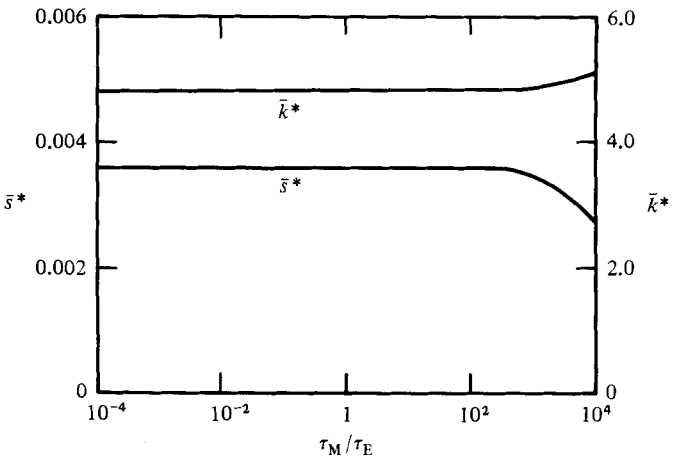

FIGURE 7. Fastest-growing wavenumber $\bar{k}^*$ and growth rate $\bar{s}^*$ as functions of τ_M/τ_E with $\bar{T}_1 = 1.75$, $\bar{J}_0 = 1.0$, and $\tau_I/\tau_E = 0.0$. For τ_M/τ_E less than about 100, fluid viscosity dominates over inertia, and k^* and $\bar{s}^*$ are independent of τ_M/τ_E. For high values of τ_M/τ_E, fluid inertia lowers $\bar{s}^*$ and increases $\bar{k}^*$.

value of the wavenumber. The cellular instability corresponding to pure real growth is analogous to that for which marginal stability conditions have been developed by Worraker & Richardson. At the high wavenumber, 'overstability', involving both growth and propagation, produces a series of slanted cells, with an associated physical mechanism similar to that encountered in ohmic liquid EHD instability analyses (Hoburg & Melcher 1976; Hoburg 1978). Cellular fluid motions lead to perturbation charge accumulation responsible for the propagation. The complex-conjugate eigenfrequency corresponds to a streamline slant which is mirrored through the vertical, and propagation in the opposite direction.

The dependence of fastest-growing eigenfrequency $\bar{s}^*$ and corresponding wavenumber $\bar{k}^*$ upon injected current density and time-constant ratios is represented in figures 6–9. In figure 6, $\bar{k}^*$ and $\bar{s}^*$ are shown as functions of injected current density, $\bar{J}_0$, for values increasing from zero to the space-charge-limited value. The wavenumber for most-rapid growth is nearly independent of injected current until $\bar{J}_0$ nears $\bar{J}_{SCL}$; $\bar{k}^*$ then decreases, corresponding to a longer instability wavelength, as $\bar{J}_0$ increases to $\bar{J}_{SCL}$. The corresponding most-rapid growth rate increases with increasing injected current, but reaches a maximum at a value of $\bar{J}_0$ less than $\bar{J}_{SCL}$. This is an important and somewhat unexpected result – instability growth is maximized by using an injected current less than the space-charge-limited value.

Figure 7 shows the dependences of $\bar{k}^*$ and $\bar{s}^*$ upon τ_M/τ_E, which is a measure of the relative importances of fluid inertia and viscosity. For values of τ_M/τ_E less than about 100, fluid motions are viscous-dominated, and $\bar{k}^*$ and $\bar{s}^*$ are independent of τ_M/τ_E. At high values of τ_M/τ_E, fluid inertia becomes significant, lowering the most-rapid growth rate and increasing the corresponding wavenumber.

Figures 8 and 9 show the dependence of $\bar{s}^*$ upon τ_I/τ_E, the 'electric Rayleigh number' parameter associated with instability incipience in the classical space charge instability process with no mobility gradient, and upon $\bar{T}_1$, the normalized upper electrode temperature. In figure 8, $\bar{s}^*$ is plotted versus τ_I/τ_E for five values of temperature gradient. The dependence here deserves emphasis, since it clarifies the nature of the two kinds of instability mechanism which are interwoven. Analysis of

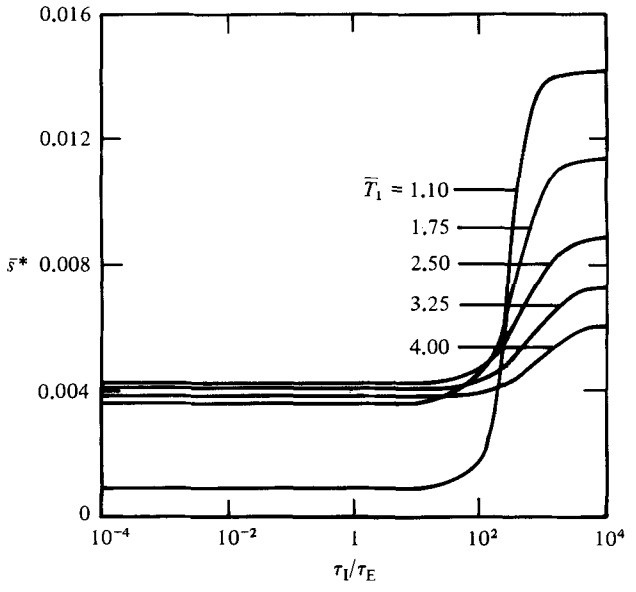

FIGURE 8. Growth rate $\bar{s}^*$ versus τ_I/τ_E at various temperature gradients with $\bar{J}_0 = 1.0$ and $\tau_M/\tau_E = 1.0$. For values of τ_I/τ_E much less than 100, where the classical space-charge instability is below incipience, the mobility-gradient-driven mechanism leads to instability. For τ_I/τ_E much greater than 100, the classical mechanism dominates.

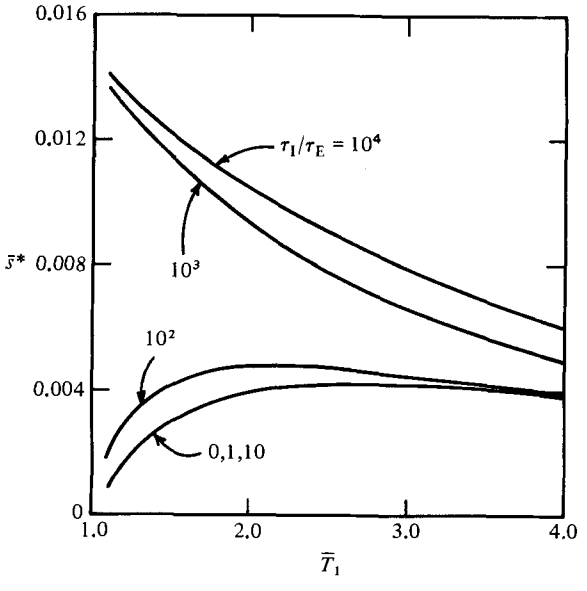

FIGURE 9. Growth rate $\bar{s}^*$ versus $\bar{T}_1$ at various values of τ_I/τ_E with $\bar{J}_0 = 1.0$ and $\tau_M/\tau_E = 1.0$ For low values of τ_I/τ_E, $\bar{s}^*$ increases rapidly with increasing $\bar{T}_1$ at small $\bar{T}_1$ owing to the increasing mobility gradient. At large T_1, $\bar{s}^*$ decreases slowly with T_1 owing to increasing fluid viscosity. For high values of τ_I/τ_E, $\bar{s}^*$ decreases with increasing $\bar{T}_1$.

the classical space-charge instability with no mobility gradient (Schneider & Watson 1970) leads to incipience at $\tau_I/\tau_E = 99$. Here, even with $\tau_I/\tau_E = 0$, the mobility-gradient-driven mechanism leads to instability. For values of τ_I/τ_E much less than the classical incipience value, instability growth rate is independent of τ_I/τ_E. When τ_I/τ_E becomes of order 100, $\bar{s}^*$ increases rapidly with τ_I/τ_E. The fact that the curves cross one another reflects the effect of the viscosity gradient upon growth rate in the high-τ_I/τ_E regime. Here, the classical space-charge instability dominates, and the effect of the mobility gradient is secondary. The simultaneous presence of both mechanisms leads to a smooth transition in growth rate from one regime to the other. The curve for $\bar{T}_1 = 4$ makes it clear that a large temperature gradient can produce instability growth at $\tau_I/\tau_E = 0$ very nearly as rapid as that occurring at τ_I/τ_E much higher than the classical incipience value.

In figure 9, $\bar{s}^*$ is plotted versus $\bar{T}_1$ for various values of τ_I/τ_E. For low values of τ_I/τ_E, where the classical space-charge instability is below incipience, growth rate increases rapidly with increasing temperature gradient for relatively small $\bar{T}_1$, where the effect of increasing mobility gradient is dominant. For relatively large $\bar{T}_1$, the corresponding increase in gas viscosity limits instability growth rate, so that $\bar{s}^*$ decreases slowly with increasing $\bar{T}_1$. For values of τ_I/τ_E well above the classical incipience, increased viscosity produces a fairly rapid falloff of growth rate with increasing temperature.

5. Discussion

The model described in the preceding sections involving a mobility gradient in a gas adjacent to a heated surface with associated alterations of charge-density and electric-field distributions, identifies the role of EHD instability in augmenting heat transfer by driving fluid motions at the scale of the mobility variation. The relationship of the mobility-gradient-driven mechanism to the classical space-charge instability is directly linked to the three time constants defined by (27).

τ_E is the so-called 'electroviscous' time associated with fluid motions driven by an electric stress and retarded by viscosity, while τ_M is a 'viscous-diffusion' time associated with the motion of mechanical disturbances through the fluid. The ratio τ_M/τ_E is familiar from studies of EHD instability in ohmic fluids. For example, if an electric field is applied normal to the initially flat interface between ohmic fluids of differing conductivities, perturbations of interfacial displacement grow at rates determined by τ_M/τ_E. This ratio measures the relative importance of fluid inertia and viscosity in limiting motions driven by charge accumulation in an applied electric field.

τ_I represents the time required for an ion with mobility b_0 to move across the distance d in a uniform electric field V/d. The 'electric Rayleigh number' τ_I/τ_E (Schneider & Watson 1970) defines incipient instability for injection of an ion flux into a constant-mobility fluid. This mechanism hinges on a 'charge-relaxation' process – a delay in the buildup of charge, as driven by redistributions corresponding to fluid motions, is essential to the instability.

Equation (26) is particularly instructive in distinguishing the two instability mechanisms. The charge-relaxation process is described by an interaction between $\rho_f b \boldsymbol{\nabla}\cdot\boldsymbol{E}$ and the convective time derivative of ρ_f. By contrast, when the mobility b is spatially varying, a term of the form $\rho_f \boldsymbol{E}\cdot\boldsymbol{\nabla} b$ leads to an alteration in charge accumulation at the scale of the mobility gradient.

The classical space-charge instability with constant mobility requires an applied

voltage high enough for $\tau_I/\tau_E = 99$. On the other hand, the mobility-gradient-driven instability occurs even in the instantaneous relaxation limit, where $\tau_I/\tau_E = 0$, and hence can occur at values of voltage much lower than necessary for incipience of the classical kind.

The Worraker & Richardson analysis of a mobility-gradient-driven instability in a liquid with no viscosity and density variation is specifically oriented to incipience of a stationary instability, and hence is based upon marginal-stability equations ($\bar{s} = 0$). Here, instability growth rate is documented as a function of wavenumber and time-constant ratios for a model appropriate to ion injection towards a heated plate in a gas, where viscosity and mobility increase while density decreases with position away from the injection electrode. The pure real growth at low wavenumbers and complex growth at high wavenumbers clarifies the nature of the 'exchange-of-stabilities' assumptions (i.e. that $\bar{s}$ is pure real when instability first occurs) of Schneider & Watson and Worraker & Richardson.

While the analysis of Worraker & Richardson identifies four combinations of temperature of the emitting electrode relative to the collector and gravitational orientation, the work described here is limited to injection through a positive mobility gradient, corresponding to the motivating heat transfer augmentation application. Extension of the present model to space-charge-limited conditions through a transformation of the governing equations forms the basis of ongoing investigations.

Some typical numerical values help to further clarify the roles of the instability processes. For ions in air, take $b_0 = 2 \times 10^{-4}$ m^2/V s, $\eta_0 = 2 \times 10^{-5}$ kg/m s, and $\rho_0 = 1$ kg/m^3. Then incipience of the classical space-charge instability requires

$$\tau_I/\tau_E = \frac{\epsilon V}{b_0 \eta_0} \approx 10^2$$

or $V \approx 50000$ V.

On the other hand, even with the voltage reduced by a factor of 100, at $V \approx 500$ V,

$$\frac{\tau_M}{\tau_E} = \frac{\rho_0 \epsilon V^2}{\eta_0^2} \approx 5000,$$

and, for a lengthscale $d \approx 10^{-2}$ m, $\tau_M = \rho_0 d^2/\eta_0 \approx 5$ s. Thus, at a voltage 100 times too low to lead to classical space-charge instability, an instability associated with and at the scale of the thermally created mobility gradient drives fluid motions in which inertia is beginning to compete with viscosity in limiting growth.

The issues described here have been sources of considerable confusion in attempts to model observed instances of electrical augmentation of heat transfer. The relevant literature contains analyses based upon the classical injection-space charge instability in situations where the mobility-gradient-driven mechanism should be expected to dominate (Velkoff 1962; Franke 1969) and explanations based upon effects, e.g. non-uniform polarization of gas molecules (Arajs & Legvold 1958; Lykondis & Yu 1963) whose magnitude cannot be large enough to yield force densities corresponding to observation.

This work was supported by National Science Foundation Grant MEA-8118449.

REFERENCES

ARAJS, S. & LEGVOLD, S. 1958 Electroconvectional heat transfer in gases. *J. Chem. Phys.* **29**, 531.

ATTEN, P. & LACROIX, J. C. 1978 Electrohydrodynamic stability of liquids subjected to unipolar injection: nonlinear phenomena. *J. Electrostat.* **5**, 439–452.

ATTEN, P. & MOREAU, R. 1970 Critère de stabilité hydrodynamique des fluides incompressibles insolants soumis à une injection unipolaire quelconque. *C. R. Acad. Sci.* **270**, 415–417.

CHATTOCK, A. P. 1899 On the velocity and mass of ions in the electric wind in air. *London, Edinburgh and Dublin Phil. Mag. and J. Sci.* **48** (294), 401–421.

COBINE, J. D. 1958 *Gaseous Conductors.* Dover.

FRANKE, M. E. 1969 Effect of vortices induced by corona discharge on free convection heat transfer from a vertical plate. *Trans. ASME* C: *J. Heat Transfer* **91**, 427.

HOBURG, J. F. 1978 Internal electrohydrodynamic instability of liquids with collinear field and conductivity gradients. *J. Fluid Mech.* **84**, 291–303.

HOBURG, J. F. & MELCHER, J. R. 1976 Internal electrohydrodynamic instability and mixing of fluids with orthogonal field and conductivity gradients. *J. Fluid Mech.* **73**, 333–351.

HOBURG, J. F. & MELCHER, J. R. 1977 Electrohydrodynamic mixing and instability induced by collinear fields and conductivity gradients. *Phys. Fluids* **20**, 903–911.

HOPFINGER, E. J. & GROSS, J. P. 1971 Charge transport of self-generated turbulence in insulating liquids submitted to unipolar injection. *Phys. Fluids* **14**, 1671–1682.

KIBLER, K. G. 1974 Electrostatic cooling of laser mirrors and windows. *Air Force Weapons Lab. Tech. Rep.*

KIBLER, K. G. & CARTER, H. G. 1974 Electrocooling in gases. *J. Appl. Phys.* **45**, 4436.

KULACKI, F. A. & DAUMENMIER, J. A. 1978 A preliminary study of electrohydrodynamic augmented baking. *J. Electrostat.* **5**, 325–336.

LINDSLEY, E. F. 1973 Incredible new probe puts the freeze on hot spots – instantly. *Pop. Sci.* (March) **202**, 26–28.

LYKONDIS, P. S. & YU, C. P. 1963 The influence of electrostrictive forces in natural thermal convection. *Int. J. Heat Mass Transfer* **23**, 853.

MCDERMOTT, J. 1971 High-voltage ionic discharges provide silent efficient cooling. *Electronic Design* (Sept.) **19** (20).

PALUEFF, K. K. 1933 Means for cooling electrical apparatus *US Patent* 1980821.

ROBINSON, M. 1961 Movement of air in the electric wind of the corona discharge. *Trans. AIEE* **80**, 143–150.

SADEK, S. E. 1969 Electrohydrodynamic augmentation of range ovens. *Tech. Rep. Dynatech Corp.*

SCHNEIDER, J. M. & WATSON, P. K. 1970 Electrohydrodynamic stability of space-charge-limited currents in dielectric liquids. I. Theoretical study. *Phys. Fluids* **13**, 1948–1954.

VELKOFF, H. R. 1962 Electrofluidmechanics: Investigation of the effects of electrostatic fields on heat transfer and boundary layers. *Propulsion Lab. Wright-Patterson AFB, Ohio, Tech. Rep.* ASE-TDR-62-650.

WATSON, P. K., SCHNEIDER, J. M. & TILL, H. R. 1970 Electrohydrodynamic stability of space-charge-limited currents in dielectric liquids. II. Experimental study. *Phys. Fluids* **13**, 1955–1961.

WEAST, R. C. (ed.) 1970 *Handbook of Chemistry and Physics.* Chemical Rubber Co.

WORRAKER, W. J. & RICHARDSON, A. T. 1979 The effect of temperature-induced variations in charge carrier mobility on a stationary electrohydrodynamic instability. *J. Fluid Mech.* **93**, 29–45.